Progress In Electromagnetics Research C, Vol. 173, 243–255, 2026

PIER C

(Received 7 July 2026, Accepted 10 August 2026, Scheduled 13 September 2026)

Multi-Objective Optimization Design of Water-Filled Submersible Permanent Magnet Synchronous Motors Incorporating Rotor Water Friction Loss

Sili Zhou[1,2,3,*], Shuo Zhou[1], Tianxiang Zhu[2], Zhonggen Wang[1], Yuanyuan Jiang[1], and Qunjing Wang[3]

[1]*School of Electrical and Information Engineering, Anhui University of Science and Technology, Huainan 232001, China*
[2]*Large-Scale Submersible Electric Pump Technology and Equipment Key Laboratory of Anhui*
Hefei Hengda Jianghai Pump Co., Ltd., Hefei 231131, China
[3]*National Engineering Laboratory of Energy-Saving Motor & Control Technology, Anhui University, Hefei 230601, China*

ABSTRACT: Rotor water friction loss is a critical determinant of the overall performance and efficiency of water-filled submersible permanent magnet synchronous motors (WSPMSMs) employed in mining applications. This study analyzes the electromagnetic performance and rotor water friction loss of a 500 kW WSPMSM using the finite element method and computational fluid dynamics (CFD), respectively. From a structural optimization perspective, the effects of the air-gap length and stator slot shape on rotor water friction loss were examined. A multi-objective optimization method incorporating rotor water friction loss was proposed, featuring variable stratification and differentiated reduction of optimization ranges. Firstly, an orthogonal array was constructed using the Taguchi method, and both electromagnetic finite element and CFD simulations were performed. Secondly, analysis of variance (ANOVA) classified design variables as significant and insignificant. Based on the multiple performance characteristic index (MPCI) analysis, the optimization ranges of two types of variables were narrowed to different extents. Finally, for significant variables, the response surface method (RSM) coupled with the non-dominated sorting genetic algorithm III (NSGA-III) was applied for precise optimization. For insignificant variables, the Taguchi method or parameter scanning was used for rapid optimization, depending on their number. By comparing the optimization results of the proposed method with those of existing methods, the effectiveness and superiority of the proposed method were verified.

1. INTRODUCTION

China has the world's third-largest coal reserves and is the largest producer of coal. Water hazards are among the five major disasteing emergency rescue equipment is crucial for preventing and controlling water hazards in coal mines. Compared with dry-type motors, water-filled submersible permanent magnet synchronous motors (WSPMSMs) adopt an internal water-cooling design that offers excellent heat dissipation and a compact structure. These motors can operate reliably for extended periods under harsh and complex underground conditions, making them a key focus in the research and application of high-power drainage equipment [2]. However, rotor water friction loss in these motors typically accounts for 60% to 90% of the total mechanical loss [3]. In addition, a strong fluid-structure interaction exists between the cooling water and rotor. The reverse torque produced by this water friction impedes rotor rotation and consequently affects the motor's electromagnetic characteristics [4]. Therefore, finding ways to effectively reduce rotor water friction loss while improving electromagnetic performance is of considerable theoretical significance and engineering value.

To date, research on the friction loss caused by the fluid in the air gap has mainly focused on mechanism analysis and formula derivation. Regarding the analysis of the mechanisms of fluid friction loss, in [5], the fluid field in the inner cavity of the submersible motor was studied, and an air-gap fluid grid model based on computational fluid dynamics (CFD) was established to explore the influence of the air gap on fluid velocity. In [6], to improve the efficiency of a water-filled submersible motor, a method of optimizing the ratio of diameter to shaft length and the motor's air-gap length was proposed to reduce water friction loss. In [7], a three-dimensional numerical simulation method and an 850QS-3200 type water-filled submersible motor were used as an example to establish a model of the turbulent flow field between the rotor and stator to study the turbulent flow regulation of the axial-flow cooling water. Regarding deriving formulas for fluid friction loss, in [8], the influence of rotor speed, air gap inlet flow velocity, and shield roughness on the air gap water friction loss was investigated for a high-speed permanent magnetic shielding motor, and the empirical formula of the friction loss coefficient for axial and rotational Reynolds numbers was obtained using the nonlinear fitting method. In [9], the quantitative and qualitative characterization of windage losses that can be generated at high speeds inside very narrow air gaps is provided, and a piecewise correlation for estimating rotor skin friction coefficient is proposed. In [10], an improved analytical model considering the cogging effect and cup-shaped rotor structure was proposed to address the large error in traditional oil friction loss calculations for oil-

* Corresponding author: Sili Zhou (szhou@aust.edu.cn).

immersed cooling wheel hub motors. In [11], the mechanism of oil frictional loss in the air gap of a wet-type permanent magnet synchronous motor was revealed, and an accurate oil frictional loss model was proposed, which featured a wide speed range and a narrow air gap. Existing research on WSPMSMs has treated flow and magnetic fields separately, without considering how changes in motor structural parameters jointly affect both magnetic and flow field characteristics.

The multi-objective optimization design of permanent magnet synchronous motors (PMSMs) has become a prominent research focus in electrical engineering. Researchers worldwide have explored novel motor structure designs to improve overall motor performance. In [12], a new surface-mounted, interior hybrid PMSM was proposed to overcome the limited field-weakening speed range of surface-mounted PMSMs and the large torque pulsation and magnetic leakage of interior PMSMs. In [13], a segmented asymmetric V-type permanent magnet structure was proposed, and the motor's optimal pole-span angle combination was determined using the Pareto frontier distribution and weight analysis method. In [14], a variable leakage flux permanent magnet synchronous motor (HPM-VLFM) with a hybrid series-parallel magnet configuration was proposed to overcome the non-adjustable field and narrow speed range of the conventional PMSM. Although these novel structures can improve overall performance, structural modifications often introduce engineering uncertainties, such as efficiency losses, reduced heat dissipation, and lower operational reliability. Moreover, their complex geometries make them difficult to manufacture and produce in large quantities. To avoid these problems, researchers worldwide have commonly optimized motor structural parameters using surrogate models combined with intelligent optimization algorithms, enhancing the overall performance. In [15], a completely novel collective behavior slime mold optimization (CB-SMO) method was proposed to optimize the outer-rotor PMSM with inner-periphery-inset-magnet (ORPMSM-IPIM) by introducing the social behavior of slime mold in a group, thereby increasing its torque-per-unit-weight performance. In [16], a ratio-parameter model for the double-layer PM rotor was developed, and meta-models constructed using Kriging were used in conjunction with an evolutionary algorithm to effectively achieve multi-objective optimization of PMSM. In [17], a multi-objective optimization method combining the Kriging model and non-dominated sorting genetic algorithm III (NSGA-III) was proposed for permanent magnet synchronous hub motor design, where parameters were classified by Pearson correlation analysis, and optimization results were verified by finite-element analysis and experiments. In [18], the rotor design of a line-starting PMSM was optimized by combining response surface methodology and multi-objective particle swarm optimization algorithm, considering the motor's saturation performance. In [19], the genetic algorithm-optimized extreme learning machine (GA-ELM) was used to fit the relationship between optimization parameters and objectives of the doubly salient electromagnetic machine (DSEM), and the multi-objective particle swarm optimization (MOPSO) algorithm was then used to obtain its optimal structure. Methods that combine surrogate models with intelligent optimization algorithms offer strong global search capabilities. However, when many optimization parameters and objectives are involved, and the search space is large, these methods require substantial computational resources and time, and they often suffer from reduced convergence accuracy. The Taguchi method is a local-optimization approach. By using orthogonal arrays to reduce the number of experiments, the optimal combination of structural parameters can be efficiently identified. However, its performance is constrained by the number of parameters and their levels. It also has limited accuracy in multi-objective optimization and lacks the ability to refine solutions iteratively. To address these limitations, researchers have developed improved versions of the traditional Taguchi method. In [20], considering the operating conditions, the rotor structure of an asymmetric interior permanent magnet machine was optimized using a combination of the Taguchi and K-clustering methods to increase the torque and reduce losses. In [21], a fuzzy inference system was introduced to convert multiple objectives into a single-objective optimization problem, and the sequential Taguchi method was used to optimize structural parameters of an interior permanent magnet synchronous motor (IPMSM) at multiple levels, thereby overcoming the limitation of the conventional Taguchi method in multi-objective and large-scale optimization. In [22], an IPMSM with a nonuniform air gap was designed; stator and rotor optimization variables were stratified; an improved iterative Taguchi method was proposed, achieving better optimization results while improving optimization efficiency. These improved Taguchi methods effectively address the traditional method's lack of continuous search capability and limited multi-objective optimization accuracy. However, they remain fundamentally discrete in optimization methods.

To address the above issues, this study takes a 500 kW mining WSPMSM as the research object and proposes a multi-objective optimization method. The main differences from existing methods are summarized as follows: (1) Existing WSPMSM studies generally analyze the magnetic field and the flow field separately, and the optimization design focuses mainly on electromagnetic performance. In contrast, this study incorporates rotor water friction loss into optimization objectives and simultaneously considers coupling effects of structural parameters on both electromagnetic and fluid performance. In this way, collaborative optimization of the two fields is achieved. (2) The Taguchi method offers high computational efficiency but limited accuracy for multi-objective optimization. Surrogate models combined with intelligent algorithms can achieve high optimization accuracy, but they consume substantial computational resources when the search space is large. In this study, significant and insignificant variables were identified through analysis of variance (ANOVA). The optimization ranges were then differentially reduced based on the multiple performance characteristic index (MPCI). The significant variables were precisely optimized using response surface methodology (RSM) combined with NSGA-III. The insignificant variables were rapidly optimized using the Taguchi method or parameter scanning. The proposed optimization method achieves both computational accuracy and efficiency.

Main contributions are summarized as follows: (1) Effects of the air-gap length and stator slot shape on rotor water friction loss were systematically investigated through CFD simulations, providing a quantitative basis for motor structural design aimed at reducing rotor water friction loss. (2) Rotor water friction loss was incorporated into the multi-objective optimization framework to achieve collaborative optimization of the motor's electromagnetic and fluid performance. (3) A variable stratification strategy and a differentiated optimization range reduction strategy were introduced. Significant variables were precisely optimized, while insignificant variables were rapidly optimized. This optimization approach effectively reduces computational cost while maintaining optimization accuracy.

The remainder of this paper is organized as follows. In Section 2, CFD simulations determine the influence of the air-gap length and stator slot shape on rotor water friction loss. Section 3 provides the proposed multi-objective optimization method in detail. Section 4 describes the motor's comparative performance analysis before and after optimization. Finally, Section 5 concludes the paper.

2. ANALYSIS OF THE EFFECTS ON ROTOR WATER FRICTION LOSS

2.1. Basic Parameters of the Motor

The motor's basic parameters were determined based on design specifications and practical application scenarios, as listed in Table 1.

TABLE 1. The motor's basic parameters.

Parameter	Value
Rated power (kW)	500
Rated voltage (V)	6000
Rated frequency (Hz)	75
Rated speed (r/min)	1500
Rated torque (N · m)	3183
Outer diameter of stator core (mm)	345

Fig. 1 illustrates the motor's two-dimensional finite element model. Based on the flow rate and head requirements of the mining submersible pump and given an inverter output frequency of 75 Hz and a rated speed of 1500 r/min, the motor's pole number was determined to be six. Drawing on the design experience of existing WSPMSMs on the market and considering both production process feasibility and manufacturing cost, a 36-slot stator was adopted. The stator winding uses a single-layer chain winding, characterized by a straightforward coil insertion process and high long-term operational reliability. The rotor adopts an interior inverted-V permanent magnet configuration, which increases the motor saliency ratio, exploits reluctance torque to enhance overload capability, and accommodates load variations caused by water level fluctuations in coal mines.

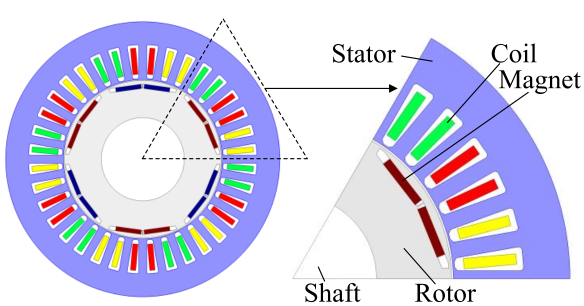

FIGURE 1. The motor's two-dimensional model.

2.2. Determination of the Flow Regime of the Air-Gap Fluid

In a WSPMSM, water fills the air gap between the stator and rotor. During motor operation, the rotating rotor drives water in the air gap, generating water friction loss. Water flow in the air gap can be either laminar or turbulent, and the corresponding loss calculation formulas differ in the two flow regimes. Under laminar flow conditions, the stator-rotor gap can be approximated as two concentric cylinders, and the water friction torque acting on the rotor is given by

$$T_{\text{wat}} = \frac{1}{2}\pi D_2^2 l_{\text{ef}} \tau \tag{1}$$

Under laminar flow conditions, the shear stress at the interface between the rotor surface and water is given by [23]

$$\tau = \frac{2\mu D_2^2 \omega}{D_{\text{i1}}^2 - D_2^2} \tag{2}$$

Therefore, rotor water friction loss is given by

$$P_{\text{wat}} = T_{\text{wat}}\omega = \frac{\pi \mu l_{\text{ef}} \omega^2 D_2^4}{D_{\text{i1}}^2 - D_2^2} = \frac{\pi \mu l_{\text{ef}} \omega^2 D_2^4}{2(D_{\text{i1}} + D_2)\delta} \tag{3}$$

where T_{wat}, ω, τ, and μ denote the water friction torque acting on the rotor, rotor angular speed, shear stress at the rotor-water interface, and dynamic viscosity of water, respectively; D_{i1}, D_2, l_{ef}, and δ are the stator inner diameter, rotor outer diameter, effective axial core length, and air gap length, respectively.

Under turbulent flow conditions, the shear stress is expressed as Eq. (4) and cannot be easily calculated analytically [23].

$$\tau = \mu \left(\frac{\mathrm{d}}{\mathrm{d}R} \bar{v}_\theta \bigg|_{R=\frac{D_2}{2}} - \omega \right) \tag{4}$$

Combining Eqs. (1) and (3) yields a general formula for the water friction loss expressed in terms of the shear stress as follows:

$$P_{\text{wat}} = \frac{1}{2}\pi D_2^2 l_{\text{ef}} \tau \omega \tag{5}$$

Therefore, under turbulent flow conditions, if the shear stress on the rotor surface can be determined, rotor water friction loss can be calculated using Eq. (5).

The water flow regime in the air gap can be determined by the Couette Reynolds number, a dimensionless parameter that characterizes the relative importance of viscous forces to inertial forces, as follows: when the Reynolds number is less than 2300, the flow is laminar, and viscous forces dominate; when it exceeds 2300, the flow is turbulent, and inertial forces dominate. The Couette Reynolds number is given by [8].

$$\mathrm{Re} = \frac{\rho v_t \delta}{\mu} \tag{6}$$

where ρ and v_t denote the water density and water tangential velocity on the rotor surface, respectively.

As shown in Table 1, for a stator inner diameter of 345 mm and a rated speed of 1500 r/min, the rotor surface linear velocities corresponding to air gap lengths of 1.6, 1.8, 2.0, and 2.2 mm are 26.84, 26.81, 26.78, and 26.75 m/s, respectively. At a water temperature of 20°C (density 998.2 kg/m^3, dynamic viscosity 1.002×10^{-3} Pa · s), Couette Reynolds numbers calculated at the rated motor speed for all air-gap lengths listed above were well above 2300, indicating turbulent flow in the air gap.

2.3. Analysis of the Effects of Air Gap Length and Stator Slot Type on Rotor Water Friction Loss

The water friction loss under rated operating conditions was calculated using CFD simulation software. Before performing the simulation, the following assumptions were made: the simulation was conducted at standard atmospheric pressure and an ambient temperature of 20°C; the stator and rotor underwent no thermal expansion, and the fluid density was treated as constant; only the steady-state flow field was investigated; there was no axial water flow at the motor inlet; only the rotation-driven motion of the water in the air gap, induced by the rotor, was considered; the rotor surface was specified as a rotating wall at the rated speed of 1500 r/min; and the surface roughness of both the stator and rotor was assumed to be constant.

The water in the air gap was treated as an incompressible Newtonian fluid, and the flow satisfied the continuity, momentum, and energy equations [24]. The rotating flow was computed using the Renormalization Group (RNG) k-ε turbulence model with standard wall functions, and all residuals were set to 10^{-5}. Due to the motor's periodic symmetry, a 1/36 section was adopted to build the fluid field model. Fig. 2 shows the air-gap fluid models for semi-closed and closed slot configurations.

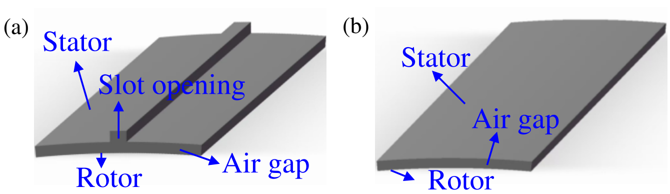

FIGURE 2. Air-gap fluid models for semi-closed slot and closed slot configurations: (a) Semi-closed slot model and (b) closed slot model.

This study adopts a combined qualitative and quantitative approach to systematically analyze the influence of the air-gap length (L_{ag}) on rotor water friction loss under two stator slot configurations, namely closed and semi-closed slots, from the perspective of motor structure optimization design. For the semi-closed slot configuration, the influence of the slot opening width (B_{s0}) and notch height (H_{s0}) on the loss was further investigated. Fig. 3 shows a schematic of structural parameters.

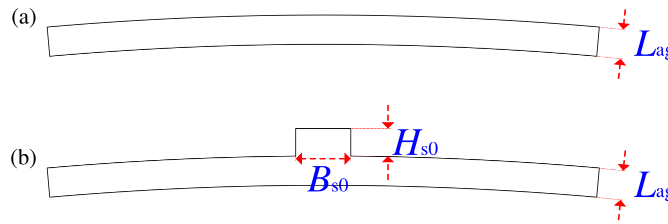

FIGURE 3. Structural parameters of semi-closed slot and closed slot air gap fluids: (a) Closed slot model and (b) semi-closed slot model.

A comparative study of the fluid field under rated conditions was conducted for closed and semi-closed slot stator configurations. For the closed slot configuration, CFD simulations were performed with L_{ag} of 1.6 mm, 1.8 mm, 2.0 mm, and 2.2 mm. For the semi-closed slot configuration, B_{s0} was fixed at 3 mm and H_{s0} at 1.5 mm, and CFD simulations were performed using the same L_{ag}. Fig. 4 shows the resulting curves of rotor water friction loss versus L_{ag} for both slot configurations. Rotor water friction loss decreased as L_{ag} increased. At the same L_{ag}, the loss with closed slots is significantly lower than that with semi-closed slots. Therefore, to reduce this loss, closed slots should be preferred in the WSPMSM design, and L_{ag} should be appropriately increased while considering the electromagnetic performance and structural feasibility.

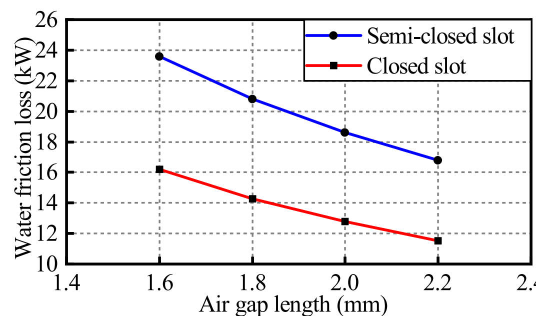

FIGURE 4. Influence of air-gap length on rotor water friction loss.

For semi-closed slots, the influence of B_{s0} on rotor water friction loss was investigated by running CFD simulations at the rated condition with L_{ag} fixed at 1.6 mm, H_{s0} at 1.5 mm, and B_{s0} set to 2.5 mm, 3.0 mm, 3.5 mm, and 4.0 mm, and Fig. 5 shows the results. The influence of H_{s0} was studied with L_{ag} fixed at 1.6 mm, B_{s0} at 3.0 mm, and H_{s0} set to 1.0 mm, 1.5 mm, 2.0 mm, and 2.5 mm, and Fig. 6 presents the results. It can be observed that, for a fixed H_{s0}, rotor water friction loss increases with B_{s0}; for a fixed B_{s0}, the loss decreases as H_{s0} increases. If design constraints require the use of semi-closed slots, B_{s0} and H_{s0} can be treated as design variables to enable co-optimizing the electromagnetic performance and rotor water friction loss. Nonetheless, the influences of B_{s0} and H_{s0} on rotor water friction loss are both weaker than those of L_{ag}.

Based on the above analysis, the motor in this study adopted closed slots to effectively reduce rotor water friction loss. To further reduce this loss and improve electromagnetic performance, rotor water friction loss, stator and rotor core losses, and permanent magnet eddy-current loss were combined into a single objective, thereby partly incorporating the interaction

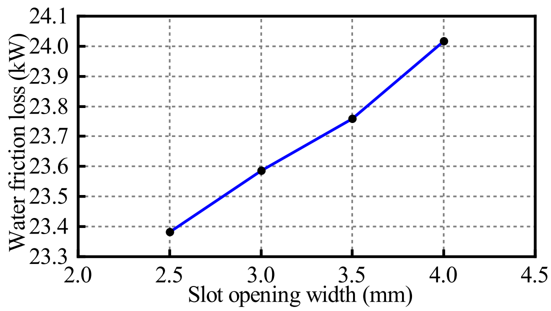

FIGURE 5. Influence of slot opening width on rotor water friction loss.

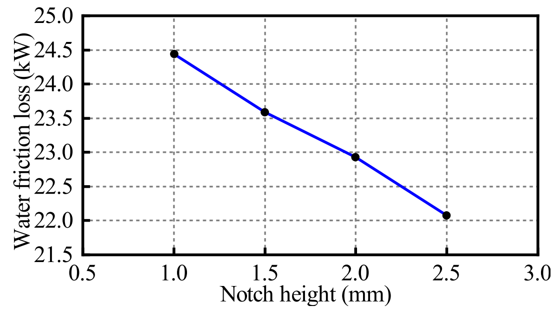

FIGURE 6. Influence of notch height on rotor water friction loss.

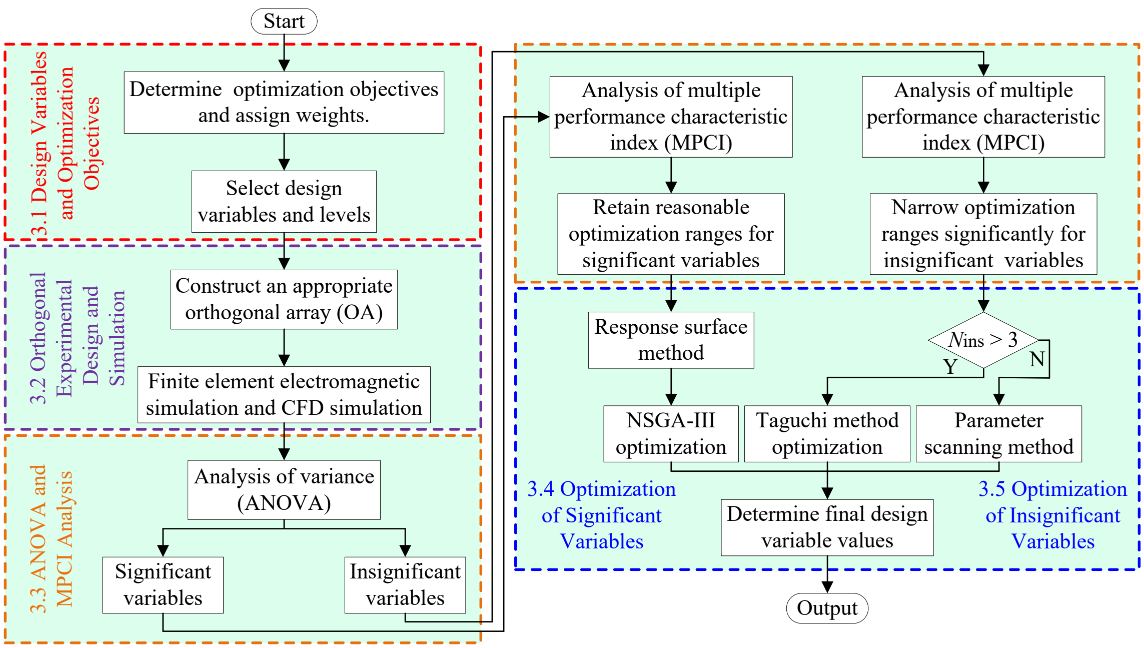

FIGURE 7. Multi-objective optimization design flowchart.

between the motor geometry and the water-filled air gap into the optimization process. This combined objective is then optimized with the relevant electromagnetic performance indicators in a multi-objective design optimization.

3. MULTI-OBJECTIVE OPTIMIZATION DESIGN OF THE MOTOR

For WSPMSMs, flow and magnetic field analyses are typically conducted independently. Existing studies rarely account for the combined influence of structural parameter variations on both magnetic and flow field characteristics. In multi-objective optimization design, too many design variables reduce efficiency, whereas too few limit design freedom and may prevent the motor from achieving optimal performance. Moreover, it is difficult to precisely determine appropriate optimization bounds for design variables: ranges that are too wide waste computational resources, whereas ranges that are too narrow risk missing the global optimum. To this end, this study proposes a multi-objective optimization method that combines variable stratification with differentiated range reduction while accounting for rotor water friction loss. Fig. 7 shows the method's detailed flowchart, where N_{ins} denotes the number of insignificant variables.

3.1. Design Variables and Optimization Objectives

To ensure a rational selection of optimization objectives, the motor's multiple performance indicators should be considered. The output torque includes average torque and torque ripple: average torque reflects the electromagnetic output capability and is a key indicator of motor load capacity, whereas torque ripple directly affects smooth operation and is closely linked to equipment reliability. Losses directly determine the operating efficiency and temperature increase, and cogging torque is a major contributor to mechanical vibration and noise. For mining WSPMSMs, the average torque (T_{avg}), torque ripple (T_{rip}), cogging torque (T_{cog}), and loss (P_{loss}) were selected as the optimization objectives. P_{loss} is defined as the sum of stator core loss, rotor core loss, permanent magnet eddy-current loss, and rotor water friction loss.

Based on weighting factors adopted in [25–28], together with the practical application requirements of mining WSPMSMs, low torque ripple is considered the primary objective, and low losses and high average torque are also required to ensure operational stability. Accordingly, the weighting factors assigned to the optimization objectives T_{avg}, T_{rip}, T_{cog}, and P_{loss} are 0.25, 0.3, 0.2, and 0.25, respectively.

Considering the slot fill factor, mechanical structure, and core saturation, the following nine structural parameters were selected as design variables: height of notch (H_{s0}), depth of slot (H_{s2}), width of slot (B_{s1}), length of air gap (L_{ag}), width of magnetic separation bridge (W_{b}), width of rotor rib (W_{r}), width of permanent magnet (W_{p}), distance from permanent magnet slot to shaft surface (D_{s}), and distance between V-shaped permanent magnet slots under the same pole (W_{s}). Fig. 8 shows the motor's detailed parametric model.

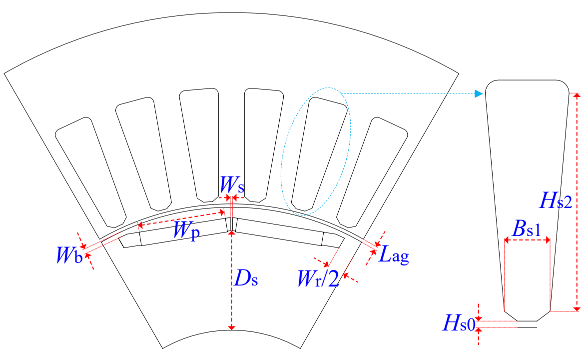

FIGURE 8. Schematic diagram of design variables for the motor.

No established formula exists for determining the initial ranges of design variables. Drawing on extensive engineering experience in motor design and analyzing the influence of each design variable on each optimization objective, this study established relatively wide initial ranges for all variables, as listed in Table 2.

TABLE 2. The motor's main design variables.

Item	Variable	Initial	Level	Value
A	H_{s0} (mm)	2	4	1–2.5
B	H_{s2} (mm)	66.25	8	65.5–67.25
C	B_{s1} (mm)	15.5	4	14–15.5
D	L_{ag} (mm)	1.8	4	1.6–2.2
E	W_{b} (mm)	1.5	4	1.5–3
F	W_{r} (mm)	18	4	16–22
G	W_{p} (mm)	57	4	57–63
H	D_{s} (mm)	66.5	4	63.5–68
I	W_{s} (mm)	3	4	1.5–3

3.2. Orthogonal Experimental Design and Simulation

Based on the number of design variables and their levels, a mixed-level orthogonal array $L_{32}(4^8, 8^1)$ was adopted for the experimental design. If a traditional full-factorial approach was used to examine all combinations of the design variable levels, it would require 524288 finite element simulations, which would be extremely time-consuming. In contrast, the Taguchi orthogonal experimental design requires only 32 simulations, substantially improving optimization efficiency and shortening the design cycle. Table 3 shows the orthogonal array and the optimization objective performance.

3.3. ANOVA and MPCI

In this study, ANOVA was used to calculate the influence proportion (P) of each design variable on optimization objectives, and the average influence proportion across all design variables, denoted as P_{avg}, is defined as 100% divided by the total number of design variables. By comparing P with P_{avg}, each design variable was classified as significant or insignificant. The classification criteria were as follows: a design variable is considered significant if its P is greater than or equal to P_{avg} for at least two optimization objectives. It is considered insignificant if its P is less than P_{avg} for all objectives, or if its P is greater than or equal to P_{avg} for only one objective.

Considering the influence proportion of design variable A on the T_{avg} as an example, ANOVA was conducted as follows:

1) The overall mean of T_{avg} across all runs of the orthogonal experiment was calculated as follows:

$$\bar{T}_{\text{avg}} = \frac{1}{32}\sum_{j=1}^{32} T_{\text{avg}\,j} \tag{7}$$

where $\bar{T}_{\text{avg}}$ represents the overall mean of T_{avg}, and j is the sample number in the orthogonal experiment.

2) Calculate the mean of T_{avg} for a single design variable at each of its levels as follows:

$$T_{\text{avg}}(A_i) = \frac{1}{m}\left[T_{\text{avg}}(1) + T_{\text{avg}}(2) + \ldots + T_{\text{avg}}(m)\right] \tag{8}$$

where $T_{\text{avg}}(A_i)$ denotes the mean of T_{avg} for design variable A at level i, and $T_{\text{avg}}(m)$ denotes the T_{avg} value from the m-th trial at level i.

3) Calculate the variance and influence proportion of this design variable for T_{avg} as follows:

$$SS_{\text{A}}(T_{\text{avg}}) = \frac{1}{k}\sum_{i=1}^{k}\left[T_{\text{avg}}(A_i) - \bar{T}_{\text{avg}}\right]^2 \tag{9}$$

$$P_{\text{A}}(T_{\text{avg}}) = \frac{SS_{\text{A}}(T_{\text{avg}})}{SS(T_{\text{avg}})} \times 100\% \tag{10}$$

where $SS_A(T_{\text{avg}})$, k, $P_A(T_{\text{avg}})$, and $SS(T_{\text{avg}})$ denote the variance of design variable A on T_{avg}, the number of levels of design variable A, the influence proportion of design variable A on T_{avg}, and the total variance of all design variables on T_{avg}, respectively. Table 4 lists the calculated results.

It can be observed that B_{s1} has a strong influence on T_{avg} and T_{cog}. L_{ag} significantly affects T_{avg} and T_{rip}, and it also contributes the most to P_{loss}. W_{b} significantly affected T_{avg} and T_{cog}, whereas W_{p} considerably influenced T_{avg}, T_{rip}, and T_{cog}.

TABLE 3. Orthogonal array and simulation results.

Number	Design variable									Optimize objective			
	A	B	C	D	E	F	G	H	I	T_{avg}	T_{rip}	T_{cog}	P_{loss}
1	1	65.5	14	1.6	1.5	16	57	63.5	1.5	3324.18	23.59	3.223	21.416
2	1	65.75	14	1.8	2	22	63	66.5	2.5	3401.46	23.74	26.046	19.864
3	1	66	14.5	2	3	16	59	66.5	3	3084.77	20.55	4.002	17.480
4	1	66.25	14.5	2.2	2.5	22	61	63.5	2	3232.22	21.38	10.758	16.416
5	1	66.5	15	1.6	2.5	18	63	65	3	3293.96	30.09	24.415	21.664
6	1	66.75	15	1.8	3	20	57	68	2	3149.10	13.78	4.298	19.338
7	1	67	15.5	2	2	18	61	68	1.5	3203.87	21.51	29.980	17.724
8	1	67.25	15.5	2.2	1.5	20	59	65	2.5	3113.66	19.21	14.111	16.248
9	1.5	66.25	14	2	3	20	63	65	1.5	3328.71	19.76	3.525	18.107
10	1.5	66	14	2.2	2.5	18	57	68	2.5	3071.88	16.28	2.404	16.657
11	1.5	65.75	14.5	1.6	1.5	20	61	68	3	3345.95	23.80	14.406	22.076
12	1.5	65.5	14.5	1.8	2	18	59	65	2	3265.42	21.04	4.307	19.566
13	1.5	67.25	15	2	2	22	57	63.5	3	3120.29	14.50	3.249	17.922
14	1.5	67	15	2.2	1.5	16	63	66.5	2	3210.27	23.65	6.453	16.648
15	1.5	66.75	15.5	1.6	2.5	22	59	66.5	1.5	3265.64	18.79	20.993	21.749
16	1.5	66.5	15.5	1.8	3	16	61	63.5	2.5	3139.73	25.79	5.050	19.413
17	2	66.5	14	2	1.5	22	59	68	2	3289.94	14.81	5.408	18.507
18	2	66.75	14	2.2	2	16	61	65	3	3154.55	18.52	0.542	16.969
19	2	67	14.5	1.6	3	22	57	65	2.5	3220.06	14.22	3.106	22.112
20	2	67.25	14.5	1.8	2.5	16	63	68	1.5	3307.91	22.69	5.633	20.077
21	2	65.5	15	2	2.5	20	61	66.5	2.5	3180.82	19.17	5.504	18.172
22	2	65.75	15	2.2	3	18	59	63.5	1.5	3095.22	16.99	1.849	16.769
23	2	66	15.5	1.6	2	20	63	63.5	2	3331.69	32.41	23.340	22.275
24	2	66.25	15.5	1.8	1.5	18	57	66.5	3	3094.14	20.83	4.608	19.769
25	2.5	67.25	14	1.6	3	18	61	66.5	2	3321.28	20.92	2.986	22.885
26	2.5	67	14	1.8	2.5	20	59	63.5	3	3232.66	17.97	1.216	20.513
27	2.5	66.75	14.5	2	1.5	18	63	63.5	2.5	3293.17	22.71	1.670	18.802
28	2.5	66.5	14.5	2.2	2	20	57	66.5	1.5	3129.79	12.86	2.320	17.371
29	2.5	66.25	15	1.6	2	16	59	68	2.5	3198.34	24.75	5.610	22.478
30	2.5	66	15	1.8	1.5	22	61	65	1.5	3339.43	22.07	11.247	20.469
31	2.5	65.75	15.5	2	2.5	16	57	65	2	3021.28	17.99	1.972	18.483
32	2.5	65.5	15.5	2.2	3	22	63	68	3	3078.88	17.12	6.539	17.170

TABLE 4. Influence proportion of design variables on the optimization objectives.

Item	Variable	Influence proportion (%)			
		T_{avg}	T_{rip}	T_{cog}	P_{loss}
A	H_{s0}	0.68	3.51	23.75	3.42
B	H_{s2}	0.07	9.12	7.25	0.10
C	B_{s1}	14.18	3.81	14.99	0.22
D	L_{ag}	27.20	22.67	9.66	95.95
E	W_{b}	23.40	5.99	12.91	0.04
F	W_{r}	4.78	11.22	9.83	0.09
G	W_{p}	22.95	38.23	17.83	0.15
H	D_{s}	0.29	4.64	2.22	0.02
I	W_{s}	6.44	0.80	1.57	0.02

In contrast, influence proportions of H_{s2}, W_{r}, D_{s}, and W_{s} for each objective were lower than P_{avg}. H_{s0} strongly affected only T_{cog}. Table 5 presents stratification results.

TABLE 5. Stratification results of design variables.

Stratification	Variable
Significant	$B_{\mathrm{s1}}, L_{\mathrm{ag}}, W_{\mathrm{b}}, W_{\mathrm{p}}$
Insignificant	$H_{\mathrm{s0}}, H_{\mathrm{s2}}, W_{\mathrm{r}}, D_{\mathrm{s}}, W_{\mathrm{s}}$

To enhance the accuracy and efficiency of the subsequent optimization, the range of each design variable must be accurately defined and narrowed. In this study, MPCI was employed to identify the preliminary optimal combination of design variables. Based on this combination, the optimization ranges of significant and insignificant variables were narrowed to different extents. The MPCI is calculated as follows:

1) Calculation of the signal-to-noise ratio (SNR) and data standardization index (DSI). To establish a unified quantitative criterion for motor optimization objectives, SNR was used as an evaluation metric in this study. T_{avg} is a larger-the-better

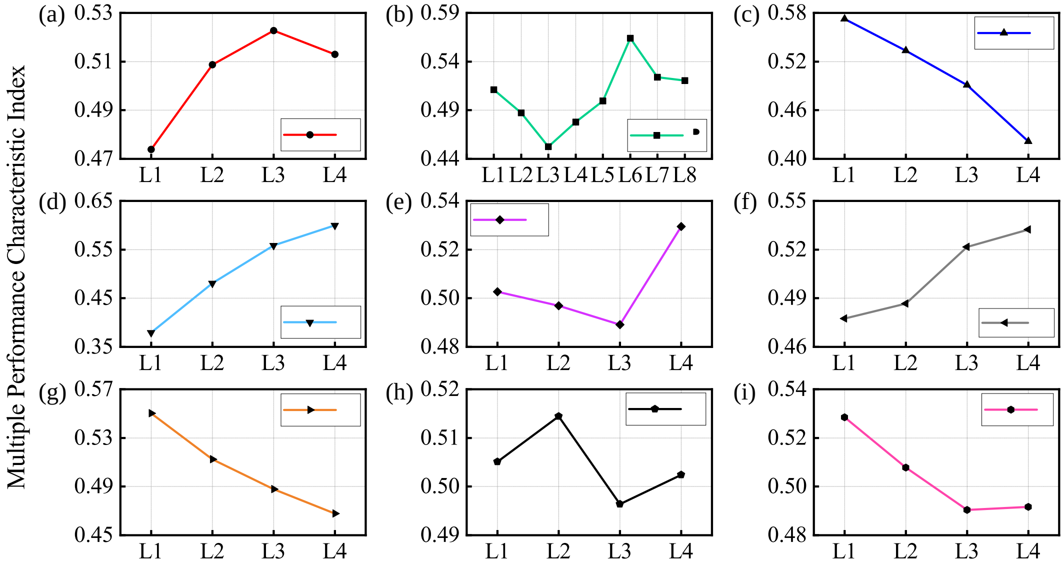

FIGURE 9. Diagram of MPCI based on each level of the design variables.

characteristic, meaning that a higher value corresponds to better motor performance. T_{rip}, T_{cog}, and P_{loss} are smaller-the-better characteristics, indicating that lower values indicate better performance. Taking the SNR calculation for T_{avg} and T_{rip} as an example, the respective formulas are as follows:

$$SNR(T_{\text{avg}}) = -10\lg\left[\frac{1}{n}\sum_{j=1}^{n}(T_{\text{avg}\,j})^{-2}\right] \tag{11}$$

$$SNR(T_{\text{rip}}) = -10\cdot\log\left[\frac{1}{n}\sum_{j=1}^{n}(T_{\text{rip}\,j})^{2}\right] \tag{12}$$

where n denotes the number of runs in the orthogonal experiment, and j denotes the sample number in the orthogonal experiment.

Based on SNR results, DSI was used to enable a more intuitive comparison. Taking the SNR of T_{avg} as an example, the DSI is calculated as follows:

$$DSI\left(T_{\text{avg}\,j}\right) = \frac{SNR\left(T_{\text{avg}\,j}\right) - \min SNR\left(T_{\text{avg}\,j}\right)}{\max SNR\left(T_{\text{avg}}\right) - \min SNR\left(T_{\text{avg}}\right)} \tag{13}$$

where $\max SNR(T_{\text{avg}})$ and $\min SNR(T_{\text{avg}})$ denote the maximum and minimum SNRs among all samples, respectively.

2) Calculation of MPCI. DSI results are integrated into the MPCI, and the MPCI for the j-th trial is calculated as follows:

$$\text{MPCI}_j = \lambda_1 DSI\left(T_{\text{avg}\,j}\right) + \ldots + \lambda_4 DSI\left(P_{\text{loss}\,j}\right) \tag{14}$$

where λ_1, λ_2, λ_3, and λ_4 denote the weighting factors of optimization objectives T_{avg}, T_{rip}, T_{cog}, and P_{loss}, respectively. Taking the calculation for design variable C at Level 1 as an example, the MPCI is calculated as

$$MPCI(C_1) = \frac{1}{8}\begin{pmatrix} MPCI_1 + MPCI_2 + MPCI_9 \\ + MPCI_{10} + MPCI_{17} + MPCI_{18} \\ + MPCI_{25} + MPCI_{26} \end{pmatrix} \tag{15}$$

Fig. 9 presents MPCI results. The preliminary optimal combination of design variables was A3, B6, C1, D4, E4, F4, G1, H2, and I1. Based on this combination, the electromagnetic finite element and CFD simulations of the motor were conducted. Table 6 shows the resulting data.

TABLE 6. Results of motor performance based on Taguchi design with MPCI analysis.

Optimize objective	Value
T_{avg} (N · m)	3144.77
T_{rip} (%)	10.28
T_{cog} (N · m)	1.943
P_{loss} (kW)	16.992

Based on the preliminary optimal combination of design variables, the optimization ranges of significant and insignificant variables were narrowed. Taking design variable A as an example, its initial levels are L_1, L_2, L_3, and L_4, and the spacing between adjacent levels is d_1. The MPCI reaches its maximum value at level L_2. The optimization range was narrowed according to the following rules:

For a significant variable, the optimization range is narrowed to $[L_2 - d_2,\ L_2 + d_2]$, where $d_2 = d_1$;

For an insignificant variable, the optimization range is narrowed to $[L_2 - d_2,\ L_2 + d_2]$, where $d_2 \leq 3d_1/5$;

The above narrowing rules must be applied on the premise that the motor structure is reasonable enough.

Fig. 10 shows narrowing rules for the optimization range. Table 7 lists optimization range narrowing results for each design variable.

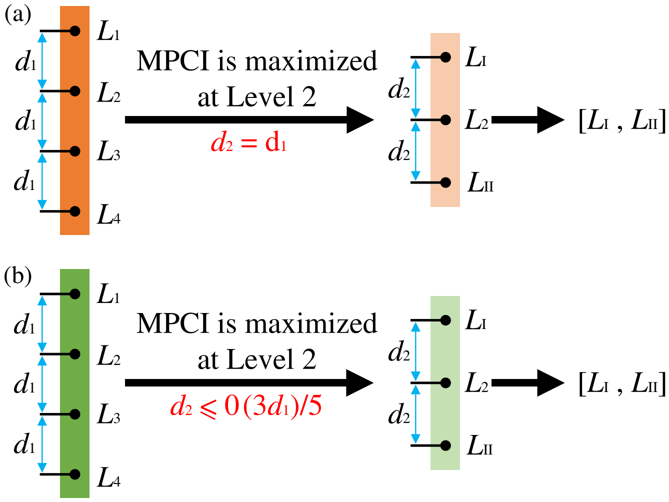

FIGURE 10. Schematic diagram of adjustment for design variables: (a) Significant variables and (b) insignificant variables.

3.4. Optimization of Significant Variables

To accurately determine the global optimum for significant variables, this study constructed second-order polynomial surrogate models for B_{s1}, L_{ag}, W_{b}, and W_{p} using RSM, and solved the models using NSGA-III. RSM approximates the objective functions, such as T_{avg} and P_{loss}, using a second-order polynomial model of the following form:

$$y = \beta_0 + \sum_{i}^{m} \beta_i x_i + \sum_{i}^{m} \beta_{ii} x_i^2 + \sum_{i<j} \beta_{ij} x_i x_j + \varepsilon \tag{16}$$

where y denotes the response value; x_i and x_j denote design variables; β_0, β_i, β_{ii}, and β_{ij} denote regression coefficients to be estimated; ε denotes the error term. Based on the Box-Behnken design (BBD), an experimental scheme is designed, and the second-order response surface models for T_{avg}, T_{rip}, T_{cog}, and P_{loss} are numerically fitted. The fitted models for these objectives are as follows:

$$\begin{aligned} T_{\text{avg}} = {} & 883.9356 + 29.4983 B_{\text{s1}} - 515.1792 L_{\text{ag}} \\ & -94.4283 W_{\text{b}} + 100.3888 W_{\text{p}} + 24.9 B_{\text{s1}} L_{\text{ag}} \\ & +4.06 B_{\text{s1}} W_{\text{b}} - 1.595 B_{\text{s1}} W_{\text{p}} - 7.2 L_{\text{ag}} W_{\text{b}} \\ & +0.8375 L_{\text{ag}} W_{\text{p}} + 0.065 W_{\text{b}} W_{\text{p}} - 2.5 B_{\text{s1}}^2 \\ & -33.5 L_{\text{ag}}^2 - 1.065 W_{\text{b}}^2 - 0.4706 W_{\text{p}}^2 \end{aligned} \tag{17a}$$

$$\begin{aligned} T_{\text{rip}} = {} & 136.2191 + 25.6783 B_{\text{s1}} + 41.4958 L_{\text{ag}} \\ & +14.8983 W_{\text{b}} - 14.149 W_{\text{p}} - 1.1 B_{\text{s1}} L_{\text{ag}} \\ & -0.18 B_{\text{s1}} W_{\text{b}} - 0.105 B_{\text{s1}} W_{\text{p}} + 1.85 L_{\text{ag}} W_{\text{b}} \\ & -1.4125 L_{\text{ag}} W_{\text{p}} - 0.295 W_{\text{b}} W_{\text{p}} - 0.56 B_{\text{s1}}^2 \\ & +11 L_{\text{ag}}^2 + 0.045 W_{\text{b}}^2 + 0.1791 W_{\text{p}}^2 \end{aligned} \tag{17b}$$

$$\begin{aligned} T_{\text{cog}} = {} & 22.3315 - 14.8208 B_{\text{s1}} + 25.8488 L_{\text{ag}} \\ & +7.1954 W_{\text{b}} + 1.1145 W_{\text{p}} - 0.38 B_{\text{s1}} L_{\text{ag}} \\ & -0.156 B_{\text{s1}} W_{\text{b}} + 0.2355 B_{\text{s1}} W_{\text{p}} + 0.215 L_{\text{ag}} W_{\text{b}} \\ & -0.4288 L_{\text{ag}} W_{\text{p}} - 0.1043 W_{\text{b}} W_{\text{p}} + 0.1233 B_{\text{s1}}^2 \\ & +0.4333 L_{\text{ag}}^2 + 0.0213 W_{\text{b}}^2 - 0.0249 W_{\text{p}}^2 \end{aligned} \tag{17c}$$

$$\begin{aligned} P_{\text{loss}} = {} & 2.1533 + 12.4262 B_{\text{s1}} - 49.3246 L_{\text{ag}} \\ & +0.2193 W_{\text{b}} - 0.5138 W_{\text{p}} - 0.68 B_{\text{s1}} L_{\text{ag}} \\ & -0.02 B_{\text{s1}} W_{\text{b}} + 0.0035 B_{\text{s1}} W_{\text{p}} + 0.245 L_{\text{ag}} W_{\text{b}} \\ & -0.1763 L_{\text{ag}} W_{\text{p}} - 0.007 W_{\text{b}} W_{\text{p}} - 0.396 B_{\text{s1}}^2 \\ & +14.8125 L_{\text{ag}}^2 - 0.023 W_{\text{b}}^2 + 0.0077 W_{\text{p}}^2 \end{aligned} \tag{17d}$$

TABLE 7. Optimization range adjustment of design variables.

Category	Item	Variable	Initial	Reduced	Value
Significant	C	B_{s1} (mm)	14–15.5	14–14.5	14
	D	L_{ag} (mm)	1.6–2.2	2–2.2	2.2
	E	W_{b} (mm)	1.5–3	2.5–3.5	3
	G	W_{p} (mm)	57–63	55–59	57
Insignificant	A	H_{s0} (mm)	1–2.5	1.7–2.3	2
	B	H_{s2} (mm)	65.5–67.25	66.61–66.89	66.75
	F	W_{r} (mm)	16–22	20.8–23.2	22
	H	D_{s} (mm)	63.5–68	64.1–65.9	65
	I	W_{s} (mm)	1.5–3	1.2–1.8	1.5

The fit of response surface models is assessed using the coefficient of determination R^2, where a value closer to 1 indicates higher accuracy. The analysis gives R^2 values of 0.9999, 0.9916, 0.9998, and 0.9909 for T_{avg}, T_{rip}, T_{cog}, and P_{loss}, respectively. All these values are close to 1, confirming that the models are properly constructed and offer high reliability and predictive accuracy.

This paper employs NSGA-III as a global optimizer to perform multi-objective optimization on fitted response surface models. The optimization parameters were set as follows: 10 reference points, a population size of 200, and 200 generations. The stopping criterion was either reaching the maximum number of generations or the change in the Pareto front across consecutive generations falling below a predefined threshold. Considering practical machining precision constraints, all design variable values were rounded to two decimal places during optimization. Fig. 11 illustrates the resulting Pareto front. On this basis, the Pareto solution set was filtered by applying constraints that incorporated some of the rated design specifications of the motor and certain simulation results from Table 6.

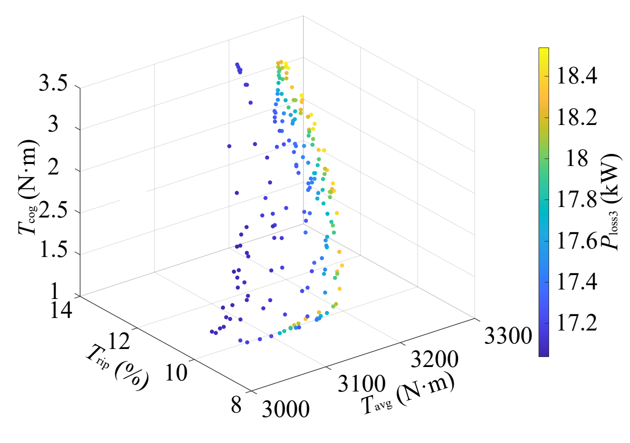

FIGURE 11. Pareto front.

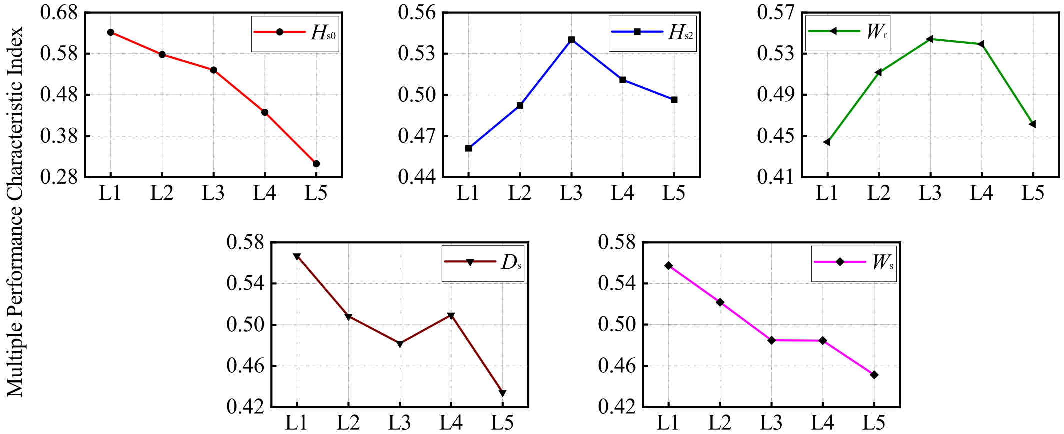

FIGURE 12. Diagram of MPCI based on each level of insignificant variables.

The corresponding constraints are expressed as follows:

$$\begin{cases} T_{\text{avg}} \geq 3183\,\text{N}\cdot\ \text{m} \\ T_{\text{rip}} \leq 10.28\% \\ T_{\text{cog}} \leq 1.943\,\text{N}\cdot\ \text{m} \end{cases} \tag{18}$$

By the MPCI analysis of filtered solutions, the final optimized values of significant variables were determined, and Table 8 shows the results.

TABLE 8. Final optimized values of significant variables.

Variable	B_{s1} (mm)	L_{ag} (mm)	W_b (mm)	W_p (mm)
Value	14	2.02	2.51	55.56

3.5. Optimization of Insignificant Variables

To obtain the optimal solution efficiently, the Taguchi method was applied to the multi-objective optimization of five insignificant variables: H_{s0}, H_{s2}, W_r, D_s, and W_s. Since the number of these variables exceeds three, this choice follows the multi-objective optimization flowchart shown in Fig. 7. Table 9 presents level values of these insignificant design variables. A standard $L_{25}(5^5)$ orthogonal array was adopted. With the significant variables held at their previously optimized values, each optimization objective was evaluated through electromagnetic finite element and CFD simulations. Fig. 12 shows MPCI analysis results for insignificant variables. Table 10 lists the optimized values of insignificant variables.

TABLE 9. Level values of insignificant variables.

Variable	Value 1	Value 2	Value 3	Value 4	Value 5
H_{s0} (mm)	1.7	1.85	2	2.15	2.3
H_{s2} (mm)	66.61	66.68	66.75	66.82	66.89
W_r (mm)	20.8	21.4	22	22.6	23.2
D_s (mm)	64.1	64.55	65	65.45	65.9
W_s (mm)	1.2	1.35	1.5	1.65	1.8

TABLE 10. Final optimized values of insignificant variables.

Variable	H_{s0} (mm)	H_{s2} (mm)	W_r (mm)	D_s (mm)	W_s (mm)
Value	1.7	66.75	22	64.1	1.2

4. PERFORMANCE VERIFICATION OF THE MOTOR

4.1. Comparative Analysis

To further validate the effectiveness of the proposed optimization method, the NSGA-III combined with the Kriging model [17] and the sequential Taguchi method [21] was employed to optimize motor performance. Table 11 lists design variable values obtained for different design schemes. Table 12 lists motor performance indicators obtained for different design schemes. Figs. 13 and 14 show torque and cogging torque waveform comparisons, respectively.

TABLE 11. Values of motor design variables under different schemes.

Variable	Initial	Taguchi	This study	Sequential Taguchi	Kriging and NSGA-III
H_{s0} (mm)	2	2	1.7	1.79	1.8
H_{s2} (mm)	66.25	66.75	66.75	66.75	66.75
B_{s1} (mm)	15.5	14	14	14	14
L_{ag} (mm)	1.8	2.2	2.02	2.02	2.02
W_b (mm)	1.5	3	2.51	2.51	2.51
W_r (mm)	18	22	22	22	22
W_p (mm)	57	57	55.56	55.54	55.54
D_s (mm)	66.5	65	64.1	64.08	64.08
W_s (mm)	3	1.5	1.2	1.21	1.22

Compared with the other two schemes (initial, Taguchi), the proposed optimization method achieves superior motor performance. In addition, compared with both the NSGA-III combined with the Kriging model and the sequential Taguchi method, the proposed method yields essentially consistent optimization results while requiring significantly less time and computational resources. This verifies the effectiveness and superiority of the proposed method.

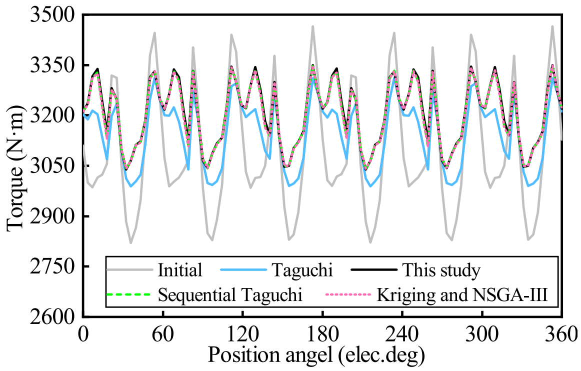

FIGURE 13. Torque comparison diagram.

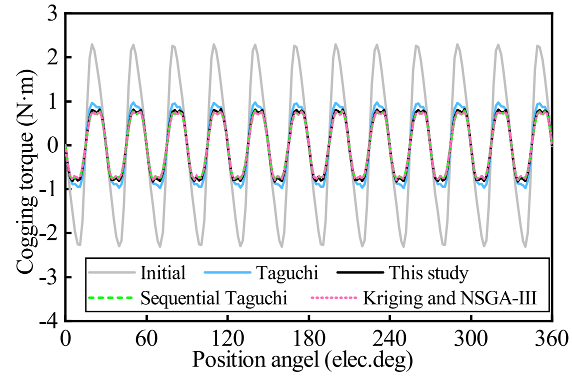

FIGURE 14. Comparison diagram of cogging torque.

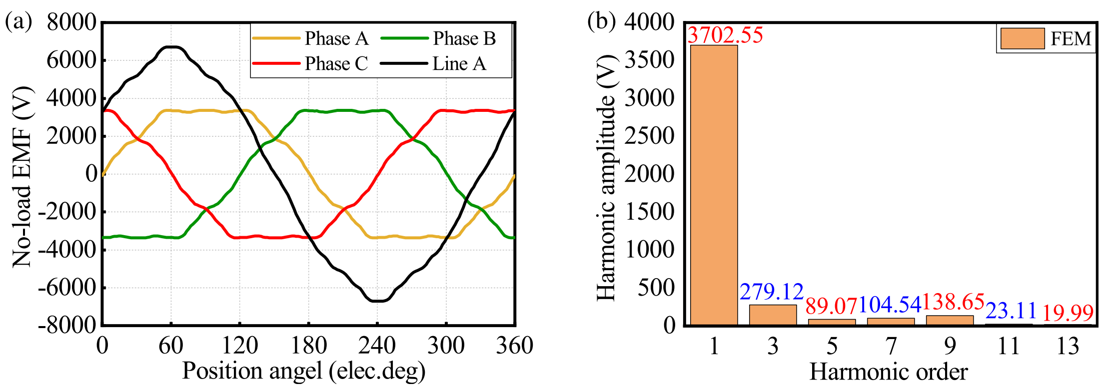

FIGURE 15. No-load back EMF and harmonic analysis: (a) Distribution and (b) harmonic content.

TABLE 12. Comparison of main motor performance indicators.

Motor performance	Initial	Taguchi	This study	Sequential Taguchi	Kriging and NSGA-III
T_{avg} $(\mathrm{N\cdot m})$	3094.14	3144.77	3206.88	3204.49	3203.43
T_{rip} (%)	20.83	10.28	9.66	9.59	9.53
T_{cog} $(\mathrm{N\cdot m})$	4.608	1.943	1.645	1.585	1.575
P_{loss} (kW)	19.769	16.992	17.951	17.999	18.015

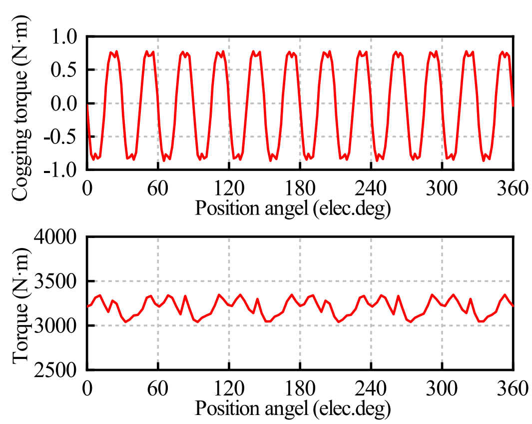

FIGURE 16. Cogging torque and output torque curves.

4.2. No-Load Analysis and Loaded Analysis

A finite element electromagnetic simulation was performed under rated no-load conditions. No-load back electromotive force (EMF) waveform and line-to-line back EMF waveform were obtained. Harmonic analysis was conducted on the A-phase back EMF over one cycle, as illustrated in Fig. 15. Calculated using Eq. (19), the total harmonic distortion (THD) of the no-load back EMF was 9.24%, and its waveform was highly sinusoidal. The root mean square (RMS) value of the line-to-line back EMF was 4538.16 V, and the peak value was 6712.89 V; both fell within the allowable design range.

$$\mathrm{THD} = \frac{U_{\mathrm{nrms}}}{U_{\mathrm{1rms}}} \times 100\% \tag{19}$$

where *THD* denotes the total harmonic distortion; U_{nrms} denotes the RMS value of the n-th harmonic; and U_{1rms} denotes the RMS value of the fundamental component.

Figure 16 presents the cogging torque curve under rated no-load conditions and the output torque curve under rated load conditions. T_{cog} is $1.645\,\mathrm{N\cdot m}$, accounting for only approximately 0.051% of T_{avg}. Therefore, its influence on output torque is negligible, which contributes to smooth motor operation with low vibration and noise. T_{avg} is $3206.88\,\mathrm{N\cdot m}$, and T_{rip} is 9.66%. Even without torque-ripple suppression methods, such as rotor skewing, stator slot skewing, or auxiliary slots on stator and rotor surfaces, this output characteristic can meet the stable output requirement of the mining WSPMSM. The optimized average torque $(3206.88\,\mathrm{N\cdot m})$ is slightly higher than the rated value $(3183\,\mathrm{N\cdot m})$. The main physical reasons are as follows: (1) Increasing W_r and decreasing W_s increase the saliency ratio (L_q/L_d), thereby enhancing the reluctance torque component. (2) Optimizing the magnetic circuit structure suppresses inter-pole flux leakage and increases the fundamental amplitude of the air-gap flux density. Although the permanent magnet width is slightly reduced, the effective air-gap flux increases, which improves permanent-magnet torque. (3) Appropriately increasing L_{ag} reduces rotor water friction loss, allowing more input power to be converted into useful output torque. (4) Optimizing the slot shape parameters suppresses the harmonic components of the air gap permeance, improves the sinusoidal waveform of the magnetic field, and reduces torque ripple and additional harmonic losses, thereby further increasing the effective average torque.

The WSPMSM;s total loss (P_{total}) comprises the winding copper loss (P_{cu}), stator and rotor core losses (P_{fe}), permanent magnet eddy current loss (P_{edd}), mechanical loss (P_{me}), and stray loss (P_s). P_{me} consists mainly of rotor water friction loss, and P_s is estimated to be 0.5% of the input power. At the rated operating point (1500 r/min, 3206.88 N · m), the calculated total loss was approximately 30.378 kW, which yielded an efficiency of approximately 93.97%.

A prototype water-pump assembly was fabricated based on the optimized structure and dimensions. Fig. 17 shows the three-dimensional geometries of the stator and rotor cores. Tests were then successfully conducted in accordance with industry practices, and all motor performance indicators met design targets.

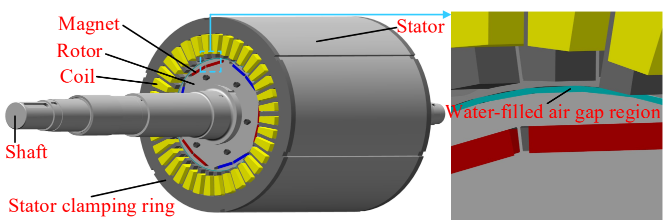

FIGURE 17. Three-dimensional geometric structure of the motor.

5. CONCLUSION

Rotor water friction loss is a critical determinant of the overall performance and efficiency of WSPMSMs in mining applications. This study investigated the effects of air-gap length and stator slot shape on rotor water friction loss using CFD simulations and proposed a multi-objective optimization design method incorporating this loss.

The analysis of rotor water friction loss showed that this loss decreased as the air-gap length increased. At the same air-gap length, the loss with closed slots was substantially lower than that with semi-closed slots. Therefore, in the WSPMSM design, closed slots should be preferred, and the air-gap length can be appropriately increased with due consideration of the electromagnetic performance and structural constraints. If the design constraints require the use of semi-closed slots, increasing the slot opening width increases rotor water friction loss, whereas increasing the notch height decreases it. However, the influence of both the slot opening width and notch height on rotor water friction loss is weaker than that of the air-gap length.

A multi-objective optimization method incorporating rotor water friction loss was proposed, featuring variable stratification and differentiated reduction of optimization ranges. By comparing the optimization results of the proposed method with those of existing methods, the effectiveness and superiority of the proposed method were verified.

This study provides an effective analysis method and optimization strategy for the high-performance design of WSPMSMs. The findings offer valuable theoretical guidance and practical reference for the engineering development of such motors and similar machines. This study focuses on optimizing the motor geometry while considering rotor water friction loss, rather than performing a complete optimization of the hydraulic or cooling system. Parameters such as coolant flow rate, inlet velocity, pressure, axial flow distribution, cooling-channel structure, and inlet-outlet configuration are not treated as design variables in this work. This assumption helps reduce the optimization complexity. Moreover, because all design schemes were analyzed under identical hydraulic and cooling boundary conditions, the model simplification error caused by neglecting variations in hydraulic and cooling parameters affects each scheme in essentially the same way. Therefore, the relative ranking among design schemes remains unchanged, and the selection of the optimal solution is not affected. However, in actual motor operation, the hydraulic and cooling system parameters influence the air-gap flow field and the wall shear stress distribution. This may lead to some deviation between the calculated rotor water friction loss and the actual value. To address this limitation, future work could incorporate hydraulic and cooling system parameters. This would make the simulations more representative of actual operating conditions and improve the results' accuracy and reliability.

ACKNOWLEDGEMENT

This work was supported in part by the Research Foundation of National Engineering Laboratory of Energy-Saving Motor & Control Technology of Anhui University under Grant KFKT202503, in part by the Research Foundation of Anhui Province Engineering Research Center of Advanced Power Electronics and Energy Conversion of Anhui University under Grant APE202505, in part by the Research Foundation of Jiangsu Engineering Research Center for Bionics Control Technology and Equipment under Grant FSKZ202503, in part by the Research Foundation of Anhui Provincial Key Laboratory of Smart Distribution Grid Operation and Control under Grant SYS-KFKT-202507, and in part by the Regional Innovation Joint Key Project of China's National Natural Science Foundation under Grant U23A20647.

REFERENCES

[1] Liu, M., W. Qiao, X. Meng, P. Feng, and X. Cheng, "A classification system for the risk assessment of roof water inrush of coal mines," *Mine Water and the Environment*, Vol. 45, 452–476, 2026.

[2] Zhang, S., H. Ren, Y. Wang, Y. Miao, Y. Shang, and Y. Feng, "Research on heat transfer of submersible motor stator based on

air gap flow characteristics," *Journal of Electromagnetic Engineering and Science*, Vol. 25, No. 2, 144–153, 2025.
[3] Tan, L., Y. Wang, Y. Wu, T. Wang, J. Cui, and H. Wang, "Research on multiphyics bidirectional coupling for small-diameter high-speed submersible permanent magnet synchronous motor," *Heliyon*, Vol. 10, No. 17, e36582, 2024.
[4] Xu, J., W. Jin, H. Guo, T. Yu, and Z. Jiao, "Design and analysis of a high-speed wet-type fault-tolerant permanent magnet motor considering oil frictional loss for aerospace electrohydrostatic actuator application," *IEEE Transactions on Transportation Electrification*, Vol. 10, No. 3, 4667–4677, 2024.
[5] Zhang, S., H. Ren, D. Zhang, S. Wang, H. Zhang, R. Luo, and Y. Feng, "Air gap fluid flow characteristics of high-power water-cooled submersible motors," *Desalination and Water Treatment*, Vol. 314, 330–338, 2023.
[6] Li, J., C. Di, and X. Bao, "Efficiency improvement for submersible motors by optimizing the ratio of diameter to shaft length," *IEEE Transactions on Magnetics*, Vol. 58, No. 2, 1–6, 2022.
[7] Zheng, X., Y. Wang, M. Jiang, and S. Zhang, "Numerical simulation of interior turbulent flow regulation of wet submersible motor," *Wireless Personal Communications*, Vol. 102, No. 2, 1443–1459, 2018.
[8] Zhang, W., Y. Hu, L. Cao, L. Zhuo, and A. Liu, "Analysis and calculation of friction loss of high-speed permanent magnetic shielding motor," *Transactions of China Electrotechnical Society*, Vol. 38, No. 12, 3122–3129, 2023.
[9] Nachouane, A. B., A. Abdelli, G. Friedrich, and S. Vivier, "Estimation of windage losses inside very narrow air gaps of high speed electrical machines without an internal ventilation using CFD methods," in *2016 XXII International Conference on Electrical Machines (ICEM)*, 2704–2710, Lausanne, Switzerland, 2016.
[10] Jiang, P., H. Li, X. Xiang, Y. Yin, and B. Yuan, "Analytical calculation of oil friction loss taking into account action of cup-shaped rotor and teeth-grooves stator," *Electric Machines and Control*, Vol. 27, No. 5, 9–19, 2023.
[11] Xu, J., W. Jin, H. Guo, T. Yu, W. Fan, and Z. Jiao, "Modeling and analysis of oil frictional loss in wet-type permanent magnet synchronous motor for aerospace electro-hydrostatic actuator," *Chinese Journal of Aeronautics*, Vol. 36, No. 11, 328–341, 2023.
[12] Xu, A., C. Huang, B. Yi, F. Wang, and Z. Liu, "Multi-objective optimization design of surface-mounted and interior hybrid permanent magnet synchronous motor," *Progress In Electromagnetics Research C*, Vol. 154, 239–248, 2025.
[13] Wang, L., X. Zhang, J. Wu, M. Wang, W. Hu, H. Geng, and X. Pang, "Multi-objective optimization design of a segmented asymmetric V-type interior permanent magnet synchronous motor," *IEEE Transactions on Magnetics*, Vol. 61, No. 1, 1–12, 2025.
[14] Yu, Z., L. Chen, F. Wu, Q. Jia, and F. Wang, "Design and analysis of a variable-flux permanent magnet synchronous motor based on a hybrid series-parallel permanent magnet system," *Progress In Electromagnetics Research C*, Vol. 170, 241–251, 2026.
[15] Verma, M., M. Sreejeth, and M. Singh, "Design optimization of OR-PMSM-IPIM using modified slime mold optimization technique for UAV application," *Electrical Engineering*, Vol. 107, No. 7, 8347–8361, 2025.
[16] Dai, L., J. Gao, S. Niu, and S. Huang, "Multi-electromagnetic performance optimization of double-layer interior permanent magnet synchronous machine," *IEEE Transactions on Industrial Electronics*, Vol. 71, No. 11, 14 535–14 545, 2024.
[17] Sun, X., N. Xu, and M. Yao, "Sequential subspace optimization design of a dual three-phase permanent magnet synchronous hub motor based on NSGA III," *IEEE Transactions on Transportation Electrification*, Vol. 9, No. 1, 622–630, 2023.
[18] Ai, M., X. Song, W. Liu, and T. Shen, "Design of multi-objective particle swarm algorithm for line-start permanent magnet synchronous motor considering saturation condition," *Transactions of China Electrotechnical Society*, Vol. 40, No. 12, 3857–3867, 2025.
[19] Jiang, S., Z. Zhang, M. Gao, X. Yang, Y. Zhao, M. Yuan, and X. Xu, "Multi-objective optimization design of doubly salient electro-magnetic machine based on hybrid machine learning and particle swarm techniques," *Electrical Engineering*, Vol. 108, No. 3, 170, 2026.
[20] Li, S., L. Wang, and X. Bao, "An asymmetric rotor interior permanent magnet mechanical design considering operating conditions," *Electrical Engineering*, Vol. 107, No. 8, 10 363–10 377, 2025.
[21] Sun, X., Z. Shi, and J. Zhu, "Multiobjective design optimization of an IPMSM for EVs based on fuzzy method and sequential Taguchi method," *IEEE Transactions on Industrial Electronics*, Vol. 68, No. 11, 10 592–10 600, 2021.
[22] Xing, Z., X. Wang, W. Zhao, X. Li, L. Xiong, and X. Zhang, "Optimization design of interior permanent magnet synchronous motor with U-shaped rotor for low-level torque ripple and electromagnetic vibration," *IEEE Transactions on Transportation Electrification*, Vol. 10, No. 1, 1995–2007, 2024.
[23] Gao, T., L. Yang, X. Yao, S. Xiao, C. Ai, and X. Kong, "Multi-objective optimization design of high-speed wet permanent magnet brushless DC motor," *Journal of Mechanical Engineering*, Vol. 61, No. 20, 339–348, 2025.
[24] Yang, G., Y. Liu, Q. Sun, J. Qiao, and T. Wang, "Numerical simulation on the flow and temperature field in the high-power motor," *IEEE Access*, Vol. 11, 82 830–82 837, 2023.
[25] Xu, R. and W. Tong, "Multi-objective hierarchical optimization of interior permanent magnet synchronous machines based on rotor surface modification," *CES Transactions on Electrical Machines and Systems*, Vol. 6, No. 4, 352–358, 2022.
[26] Hua, Y., H. Zhu, M. Gao, and Z. Ji, "Multiobjective optimization design of permanent magnet assisted bearingless synchronous reluctance motor using NSGA-II," *IEEE Transactions on Industrial Electronics*, Vol. 68, No. 11, 10 477–10 487, 2021.
[27] Zhang, B., J. Zhao, Y. Xia, and X. Zhu, "Research on a two-stage multi-objective optimization design method for permanent magnet synchronous motors utilizing partial correlation coefficients for parameter screening," *IEEE Access*, Vol. 13, 143 479–143 488, 2025.
[28] Zhu, X., S. Li, S. Zheng, L. Quan, D. Fan, X. Zeng, and C. H. T. Lee, "Torque component redistribution and enhancement for hybrid permanent magnet motor with permanent magnet offset placement," *IEEE Transactions on Transportation Electrification*, Vol. 9, No. 1, 631–641, 2023.